Dorsal/NF-κB exhibits a dorsal-to-ventral mobility gradient in the Drosophila embryo

Hadel Al Asafen[a,1], Natalie M. Clark[b,1], Thomas Jacobsen[a], Rosangela Sozzani[b], and Gregory T. Reeves[a,2]

[a] Department of Chemical and Biomolecular Engineering, North Carolina State University, Raleigh, NC 27606

[b] Department of Plant and Microbial Biology, North Carolina State University, Raleigh, NC 27606

[1] These authors contributed equally to this work

[2] To whom correspondence should be addressed. Email: gtreeves@ncsu.edu

Abstract

Morphogen-mediated patterning is a highly dynamic developmental process. To obtain an accurate understanding of morphogen gradients, biophysical parameters such as protein diffusivities must be quantified *in vivo*. The dorsal-ventral (DV) patterning of early *Drosophila* embryos by the NF-κB homolog Dorsal (Dl) is an excellent system for understanding morphogen gradient formation. Dl gradient formation is controlled by the inhibitor Cactus/IκB (Cact), which regulates the nuclear import and diffusion of Dl protein. However, quantitative measurements of spatiotemporal Dl movement are currently lacking. Here, we use scanning fluorescence correlation spectroscopy to quantify the mobility of Dl. We find that the diffusivity of Dl varies along the DV axis, with lowest diffusivities on the ventral side, and the DV asymmetry in diffusivity is exclusive to the nuclei. Moreover, we also observe that nuclear export rates are lower in the ventral and lateral regions of the embryo. Both cross correlation spectroscopy measurements and a computational model of Dl/DNA binding suggest that DNA binding of Dl, which is more prevalent on the ventral side of the embryo, is correlated to a lower diffusivity and nuclear export rate. We propose that the variation in Dl/DNA binding along the DV axis is dependent on Cact binding Dl, which prevents Dl from binding DNA in dorsal and lateral regions of the embryo. Thus, our results highlight the complexity of morphogen gradient dynamics and the need for quantitative measurements of biophysical interactions in such systems.

Significance Statement

Tissues in developing organisms are patterned through signaling mechanisms that utilize morphogen concentration gradients. To better understand how these gradients form and are maintained, biophysical parameters such as protein diffusivities must be quantified *in vivo*. Here, we use scanning fluorescence correlation spectroscopy to quantify the mobility of the morphogen Dorsal (Dl) in the Drosophila embryo. We find that both the diffusivity and nuclear export rate of Dl varies along the dorsal-to-ventral axis, with the lowest values on the ventral side. Moreover, incorporating these experimentally determined diffusion coefficients into a mathematical model suggests that DNA binding of Dl correlates with lower Dl movement. Thus, our results highlight how quantitative measurements of biophysical parameters can improve our understanding of morphogen gradient dynamics.

Introduction

Tissues in a developing organism are patterned by short and long-range signaling achieved through morphogen concentration gradients, which carry the positional information necessary to control gene expression in a spatially-dependent fashion. In the past two decades, studies using GFP-tagged morphogens -- including early Drosophila morphogens Bicoid and Dorsal; Dpp in the wing imaginal disc; and the Hedgehog, Wnt, and TGF-β families in vertebrates -- have revealed that the establishment of morphogen gradients is a highly dynamic and complex process (Delotto et al., 2007; Entchev et al., 2000; Gregor et al., 2007; Holzer et al., 2012; Luz et al., 2014; Reeves et al., 2012; Ribes et al., 2010; Teleman and Cohen, 2000; Wallkamm et al., 2014; Wartlick et al., 2011; Williams et al., 2004; Zhou et al., 2012). Live imaging studies have challenged the established view that tissue patterning relies on a constant, steady-state level of signaling to regulate gene expression (Aldaz et al., 2010; Ashe and Briscoe, 2006; Dresch et al., 2013; Gurdon and Bourillot, 2001; Gurdon et al., 1995; Jaeger et al., 2004; Mavrakis et al., 2010; Oates et al., 2009; Pantazis and Supatto, 2014; Reeves et al., 2005; Wharton et al., 2004). To move toward a quantitative understanding of morphogen signaling, several key biophysical parameters related to gradient formation, including movement through tissues and the effect of receptor binding on nuclear import/export rates, must be measured.

Dorsal (Dl), one of three homologs to mammalian NF-κB (Steward, 1987), acts as a morphogen to pattern the dorsal-ventral (DV) axis. Dl is initially distributed uniformly along the DV axis (Roth et al., 1989; Steward et al., 1988). After the 9th nuclear division cycle, when the nuclei migrate to the periphery of the syncytial embryo, Dl begins to accumulate in ventral nuclei, and is excluded from dorsal nuclei (Roth et al., 1989; Steward et al., 1988). This DV gradient in Dl nuclear concentration is due to signaling through the Toll receptor on the ventral side of the embryo (Anderson et al., 1985a, 1985b; Belvin and Anderson, 1996). In the absence of Toll signaling, Dl remains bound by the cytoplasmic tethering protein Cactus, the *Drosophila* IκB homolog (Geisler et al., 1992; Kidd, 1992), and thus localized to the cytoplasm (Belvin et al., 1995; Bergmann et al., 1996; Reach et al., 1996; Whalen and Steward, 1993). On the ventral side, Toll signaling acts through Pelle kinase to phosphorylate Cactus (Cact), which causes dissociation of the Dl/Cact complex and degradation of Cact (Daigneault et al., 2013). Once freed from binding to Cact, Dl enters the nucleus and regulates the expression of more than 50 target genes, which initiate further signaling pathways and specification of the embryo's germ layers (Chopra and Levine, 2009; Moussian and Roth, 2005; Reeves and Stathopoulos, 2009; Stathopoulos and Levine, 2002, 2004). Toll signaling also phosphorylates Dl, which has been shown to increase Dl nuclear localization (Drier et al., 2000, 1999; Gillespie and Wasserman, 1994; Whalen and Steward, 1993). Thus, even in the absence of Cact, a shallow Dl nuclear concentration gradient is established (Bergmann et al., 1996; Cardoso et al., 2017; Roth et al., 1991).

While this well-established mechanism rapidly initiates Dl gradient formation, recent work has revealed complex dynamics in the further maturation of the gradient. In particular, live imaging of

fluorescently-tagged Dl proteins has shown that the Dl nuclear gradient grows slowly during interphase and collapses during mitosis (Delotto et al., 2007; Reeves et al., 2012). Quantification of the gradient levels has shown that, over the course of nuclear cycle 10-14, Dl (both nuclear and cytoplasmic) accumulates on the ventral side of the embryo, causing the spatial peak of the Dl gradient to grow steadily over time (Carrell et al., 2017; Liberman et al., 2009; O'Connell and Reeves, 2015; Reeves et al., 2012). In particular, diffusion and nuclear capture of Dl, both of which are regulated by Cact, are proposed to control the continuous growth of the Dl gradient peak (Carrell et al., 2017). However, the diffusivity and nuclear transport rates are not quantitatively known. Therefore, to fully understand the dynamics of Dl gradient formation, measurements of the biophysical parameters of Dl mobility (specifically diffusivity and nuclear transport rates) are needed.

Here we use scanning fluorescence correlation spectroscopy (scanning FCS) methods to measure the diffusivity and nuclear transport of Dl in live embryos. Scanning FCS techniques involve rapid and repeated acquisition of fluorescent imaging data using confocal microscopy. First, we use one scanning FCS method called Raster Image Correlation Spectroscopy (RICS) to autocorrelate GFP-tagged Dl over space and time in a small region of the embryo (Digman et al., 2005a, 2005b). Statistics of this autocorrelation function are then analyzed to infer protein diffusion, which reveals that the diffusivity of Dl-GFP varies along the DV axis. In addition, we use Pair Correlation Function (pCF) to calculate the correlation between two pixels along a line scan and visualize barriers to Dl movement (Digman and Gratton, 2009; Hinde et al., 2010). By combining pCF with Fluorescence Recovery After Photobleaching (FRAP), we show that the nuclear export rate also varies along the DV axis. RICS and pCF data on mutants that mimic the Dl gradient at different DV positions support these results. Cross-correlation RICS (ccRICS), which uses two different fluorophores (GFP and RFP, in this case), and modeling of DNA/Dl/Cact interactions suggest that the DV variation in both diffusivity and nuclear export rate is the result of a higher fraction of Dl binding to the DNA on the ventral side than on the dorsal side. Thus, by incorporating experimentally determined parameters into our mathematical model, we show that regulation of Dl nuclear transport is important for maintaining the DV gradient in Dl diffusivity.

Results

Quantification of Dl Diffusivity Reveals a Dorsal-to-Ventral (DV) Gradient
To measure the diffusivity of Dl in the embryo, we performed Raster Image Correlation Spectroscopy (RICS) analysis on embryos carrying a monomeric GFP-tagged Dl and an H2A-RFP construct in a Dl heterozygous background (hereafter referred to as Dl-GFP embryos). We performed RICS analysis (n = 150 total number of images) on nuclear cycle 12-14 embryos, when the Dl gradient is clearly defined and detectable. Specifically, we rapidly imaged small (pixel size ≤ 0.1 µm) regions of the ventral, lateral, or dorsal portions of the embryo, which have differing levels of nuclear versus cytoplasmic Dl-GFP fluorescence (Fig. 1A, Fig. S1A-D and Movies S1-3). To infer the diffusivities from these raster scans, we calculated a 3D autocorrelation function

(ACF; Fig. 1B and Equation 1 in Materials and Methods) that has a fast (ξ) and slow (η) direction due to the rapid movement and line retracing of the confocal scan, respectively (Fig. 1B,C). We then fit a one-component diffusion model to this ACF (see Fig. 1C and Equation 2 in Materials and Methods). We found that the Dl diffusion coefficient varied with the position along the DV axis, with the diffusion coefficients being lowest on the ventral side of the embryo (D = 1.1 $\pm$ 0.8 μm^2/s) and higher in lateral (2.3 $\pm$ 0.3 μm^2/s) and dorsal (2.2 $\pm$ 0.7 μm^2/s) regions (Fig. 1D). To test whether this trend is statistically significant, we used linear regression, and found the slope of the diffusion coefficient from ventral-to-dorsal (Fig. 1D) to be significantly different from zero (p-value 2×10^{-7}, r^2 value 0.33). Given that on the ventral side of the embryo Dl is predominantly nuclear, while on the dorsal side Dl is predominantly cytoplasmic, it is possible that the spatial variation in the diffusivity arises from differences in the behavior of nuclear and cytoplasmic Dl. Therefore, we calculated the autocorrelation function (ACF) for the nuclei and the cytoplasm separately. We found a ventral-to-dorsal trend (p-value 4×10^{-8}, r^2 value 0.39; Fig. 1E) in the diffusivity of nuclear-localized Dl-GFP (ventral: 0.7 $\pm$ 0.8 μm^2/s; lateral: 1.7 $\pm$ 0.4 μm^2/s; dorsal: 2.6 $\pm$ 1.6 μm^2/s). However, the cytoplasmic diffusivities (ventral: 2.0 $\pm$ 0.7 μm^2/s; lateral: 2.7 $\pm$ 0.5 μm^2/s; dorsal: 2.2 $\pm$ 0.6 μm^2/s) showed no statistically significant trend in spatial variation (p-value 0.13, r^2 value 0.034; Fig. 1F). These results suggest that the observed gradient in Dl movement is specific to nuclear-localized Dl.

We reasoned that the gradient in movement of nuclear-localized Dl could be dependent on Toll signaling, which phosphorylates Dl and increases its affinity for the nucleus (Drier et al., 2000, 1999; Gillespie and Wasserman, 1994; Whalen and Steward, 1993). To this end, we performed RICS analysis on three mutant lines with "ventral-like" ($Toll^{10B}$; Schneider et al., 1991), "lateral-like" ($Toll^{r4}$; Schneider et al., 1991), or "dorsal-like" ($pll^{2/7}$; Anderson and Nüsslein-Volhard, 1984) levels of nuclear Dl-GFP (Fig. S1E-G). If the spatial gradient in Dl movement depends on Toll signaling, then we would expect $Toll^{10B}$ embryos to have the lowest diffusivity, while $Toll^{r4}$ and $pll^{2/7}$ embryos would have higher diffusivity. Accordingly, we found the diffusivity of total (nuclear + cytoplasmic) Dl-GFP is correlated to the extent of Dl nuclear localization across the mutants ($Toll^{10B}$: 1.5 $\pm$ 0.8 μm^2/s; $Toll^{r4}$: 2.4 $\pm$ 0.6 μm^2/s; $pll^{2/7}$: 2.7 $\pm$ 0.6 μm^2/s; Fig 1D, right side). Additionally, linear regression revealed a ventral-to-dorsal trend (p-value 2×10^{-8}, r^2 value 0.35; Fig 1C). Similarly, the diffusivity of nuclear Dl-GFP varies across the mutants ($Toll^{10B}$: 0.9 $\pm$ 0.7 μm^2/s; $Toll^{r4}$: 1.4 $\pm$ 1.1 μm^2/s; $pll^{2/7}$: 3.1 $\pm$ 1.6 μm^2/s; Fig 1E) with a statistically significant trend (p-value 2×10^{-6}, r^2 value 0.32). While we did see a variation in cytoplasmic Dl-GFP diffusivity in the mutants ($Toll^{10B}$: 2.1 $\pm$ 0.8 μm^2/s; $Toll^{r4}$: 2.6 $\pm$ 0.6 μm^2/s; $pll^{2/7}$: 2.6 $\pm$ 0.7 μm^2/s; Fig 1F), the trend was weak (p-value 0.01, r^2 value 0.08), suggesting that the difference in total Dl-GFP is predominantly due to changes in nuclear diffusivity of Dl-GFP. Taken together, our RICS data on both wildtype and mutant embryos show that the diffusivity of nuclear Dl is highly correlated to the spatial gradient in Toll signaling, while the diffusivity of cytoplasmic Dl is largely unaffected by Toll signaling.

Dl Exhibits DV Variation in Nuclear Export Rate Constant

Our RICS analysis revealed that Dl movement is lowest on the ventral side, where it is primarily nuclear localized, and highest on the dorsal side, where it is primarily cytoplasmic. Thus, we reasoned that nuclear import and export rates of Dl could also vary spatially. First, to determine whether there is spatial variation in Dl movement into or out of the nucleus, we used Pair Correlation Function (pCF) analysis to measure any restriction of movement of Dl-GFP across the nuclear envelope. In contrast to RICS, which uses raster scans of the embryo, pCF requires a line scan across the nucleus (Fig. 2A, top row). Pixels outside and inside of the nucleus are then correlated one pair at a time to calculate the pCF carpet (Fig. 2A, bottom row), which is then used to determine if Dl-GFP can cross the nuclear envelope. We specifically calculated the Movement Index (MI) for each embryo, which represents the degree of Dl-GFP movement across the nuclear envelope. A high movement index suggests that Dl-GFP can cross the nuclear envelope, which is represented by an arch in the pCF carpet (demarcated by orange, dashed lines in Fig. 2A). In contrast, a low movement index suggests that Dl-GFP movement into or out of the nucleus is blocked, which is represented by a fully black column in the pCF carpet (demarcated by green, solid lines in Fig. 2A). We separated our images into two groups, those with high movement (MI > 0.5) and those with low movement (MI ≤ 0.5). We found that Dl-GFP is able to move into the nucleus across the spatial regions of the embryo, as the ventral, lateral, and dorsal regions all have a majority of images with high MI values (ventral: 92.86%; lateral: 94.44%; dorsal: 100.00%) (Fig. 2B). However, the ventral and lateral regions have significantly fewer images with high MI values when Dl-GFP is measured leaving the nucleus (ventral: 64.29%; lateral: 72.22%; p<0.07, Chi-squared test with likelihood ratio), suggesting that Dl-GFP movement out of the nucleus is restricted in the ventral and lateral regions of the embryo (Fig 2B). In contrast, on the dorsal side of the embryo, almost all of the images measuring Dl-GFP movement out of the embryo have high MI values (94.44%). To test whether this restricted movement out of the nucleus may be dependent on Toll signaling, we also performed pCF analysis in $Toll^{10B}$, $Toll^{r4}$, and $pll^{2/7}$ mutant lines (Fig. S2A), and similarly found that a lower proportion of images in "ventral-like" mutants have high MI indices when Dl-GFP movement is measured out of the nucleus ($Toll^{10B}$: 96.15% in versus 72.73% out; p<0.05, Chi-squared test with likelihood ratio) (Fig 2B). This suggests that the lower diffusivity of Dl-GFP in ventral and lateral nuclei is due to a restriction of Dl movement out of the nucleus, and this restriction of nuclear export rate correlates with the spatial gradient in Toll signaling.

While pCF analysis suggests that the Dl-GFP nuclear export rate is lower on the ventral side of the embryo, this method does not quantify the nuclear import and export rates. Thus, to provide an independent measure of the nuclear import and export rates, we also performed Fluorescence Recovery After Photobleaching (FRAP) experiments on either the ventral or dorsal sides of the embryo (Fig. 2C; see also Fig. S2B,C and Movies S4-S5). We found that the nuclear export rate, k_{out}, was significantly lower on the ventral side (0.14 ± 0.09 min^{-1}) than on the dorsal side (0.56 ± 0.29 min^{-1}; p-value 0.007; Fig. 2D). However, the nuclear import rate was not significantly

different on the two sides of the embryo (ventral: 0.31 ± 0.2 min^{-1}; dorsal: 0.40 ± 0.3 min^{-1}; p-value 0.3; Fig. 2D). Thus, our pCF results, combined with our FRAP measurements, suggest there is a mechanism that maintains Dl nuclear localization on the ventral side of the embryo.

Dorsal movement is anti-correlated with DNA binding

One possible explanation for our findings that both the nuclear diffusivity and nuclear export rate of Dl-GFP varies with position along the DV axis is that there is a substantial pool of Dl-GFP bound to DNA on the ventral side of the embryo. To determine whether such a pool exists, we used cross-correlation RICS (ccRICS; Digman et al., 2009) to measure the extent to which Dl (Dl-GFP) and Histone (H2A-RFP) may be bound to the same physical structure (in this case, DNA). We found that the ratio of the cross-correlation function (CCF) amplitude to the ACF amplitude (Fig. 3A,B), which is a relative measure of the degree to which Dl-GFP and H2A-RFP are correlated, varies along the DV axis (Fig. 3C; Digman et al., 2009). In some cases with high amplitude ratios, the overlap between Dl-GFP and H2A-RFP can be seen visually (Fig. S3A and Movie S6). In wildtype embryos, the ratio of amplitudes is significantly higher on the ventral side (0.24 ± 0.21) than in the lateral (0.11 ± 0.14) or dorsal (0.05 ± 0.14) regions of the embryo (p-value 3×10^{-4}, r^2 value 0.18 Fig. 3C). Furthermore, in both the lateral and dorsal regions, the correlation between histone and Dl is indistinguishable from zero. In these cases, the low correlation can be seen as the lack of peak in the CCF (compare Fig. S3B to S3C). In mutant embryos, the ratio of amplitudes is also anti-correlated with the levels of Toll signaling (*Toll^{10B}*: 0.4 ± 0.3; *Toll^{r4}*: 0.1 ± 0.2; *pll$^{2/7}$*: -0.05 ± 0.4; Fig 3C) with a statistically significant trend (p-value 4×10^{-7}, r^2 value 0.29). Furthermore, the ratio of amplitudes is indistinguishable from zero in *pll$^{2/7}$* mutants. The ratio of amplitudes is also negatively correlated with diffusivity, which implies that, when Dl-GFP is more strongly associated with the same physical structure as H2A-RFP (high CCF to ACF ratio), the diffusivity of Dl-GFP is lower (p-value 3×10^{-7}, r^2 value 0.16; Fig 3D). Overall, the finding that the cross correlation between Dl-GFP and H2A-RFP is negatively correlated to diffusivity suggests that DNA binding of Dl may be responsible for its lowered diffusivity and lowered nuclear export rate on the ventral side of the embryo.

Modeling predicts Dl/DNA binding lowers the average diffusivity of Dl

Our cross-correlation results suggest that the spatial variation in Dl movement could be due to a population of Dl that is bound to DNA. Given our RICS and pCF results that Dl movement is slower on the ventral side of the embryo, we further reasoned that the DNA-bound Dl has a slower diffusion coefficient than the cytoplasmic Dl. Thus, to test if the spatial variation in Dl movement is due to DNA binding, we compared two diffusion models. The first is a one-component model that has only one parameter that can be varied to fit the model to the data, which is the diffusivity of Dl (Equation 2). This one-component model assumes all Dl is freely diffusible, and that none is bound to DNA. Further, the one-component model was used to fit the ACFs from RICS and infer the diffusion coefficients of Dl-GFP shown in Fig. 1. The second model is a two-component diffusion model (Equations S32-S35) in which nuclear Dl could be in two states: freely diffusible

and DNA-bound (Fig. 4A; see Supplemental Methods for more information). The two-component model contains two additional parameters that are allowed to vary: the rate constants of DNA binding (k_{on}) and dissociation (k_{off}). We first tested if fitting a one-component model to a two-component system accurately recapitulates the experimentally determined average diffusion coefficient, as the previous RICS analysis assumed a one-component model (Fig. 1D-F). We found that fitting the one-component model to a simulated two-component autocorrelation function (ACF) yields an average diffusivity between zero and 2.3 μm^2/s, which is similar to the range of our experimentally determined values from RICS. Further, we found the average diffusivity to be strongly correlated with the simulated fraction of Dl bound to DNA in the two-component model, which is 1-φ (Fig. 4B,C and Fig. S4A-F; see Materials and Methods section for definition of φ). When a large fraction of Dl is diffusible (φ = 0.9; Fig 4B), the one component model fits the data well and predicts a reasonable diffusivity (D = 1.4 μm^2/s; Fig 4B). On the other hand, when Dl is largely bound to DNA (φ = 0.3; Fig 4C), the one component model predicts a very low diffusivity (D = 0.028 μm^2/s; Fig 4C). This low diffusivity correlates with the two slices of the ACF (the fast and slow direction) collapsing onto each other (Fig 4C and Fig. S4A,B,F). This suggests that the lower diffusion values observed on the ventral side of the embryo could be due to a large proportion of DNA-bound Dl. In support of this, when we fit the two-component model to our experimental ACFs, the two-component model fits the ACFs better than the one-component model (Fig. 4D). Taken together, these results suggest that our experimental data are indicative of a two-component system where a proportion of Dl is bound to DNA.

Finally, we used our one- and two-component models to determine if the low average diffusivity measured in the one-component model correlates with a high proportion of DNA-bound Dl in the two-component model. Accordingly, we found that, when the one component model predicts a low diffusivity, the two component model predicts a high fraction of DNA-bound Dl (p-value 9×10^{-9}, r^2 value 0.48; Fig. 4E). These results are also observed in a three component model of free Dl, Dl/Cact complex, and an immobile Dl/DNA complex (see Fig. S4G-M and Supplemental Experimental Procedures), suggesting that the nuclear Dl bound to Cact could mechanistically explain the DV asymmetry in the ability of Dl to bind DNA. In summary, our multiple component modeling shows that Dl binding to DNA only on the ventral side of the embryo could explain the DV asymmetry in Dl mobility.

Discussion

In this study, we used fluorescence fluctuation spectroscopy methods, as well as photobleaching experiments, to quantify the movement of a GFP-tagged Dl protein in the 2-3 hr old *Drosophila* embryo (Fig. 5A). Our measurements ultimately revealed a DV asymmetry in the mobility of Dl, which was correlated to a similar DV asymmetry in the ability of Dl to bind to DNA. First, RICS analysis showed that Dl diffusivity varies along the DV axis, in particular within the nucleus (Fig. 5B). Moreover, the results obtained from the pCF and FRAP experiments showed that there is also variation in the movement of Dl out of the nuclei: on the ventral side, nuclear export of Dl is not

as rapid as it is on the dorsal side (Fig. 5C). Given that our measurements show variation in the mobility of Dl along the DV axis, and that the variation is associated with nuclear-localized Dl, we hypothesized that Dl is binding more efficiently to the DNA on the ventral side than on the dorsal side (Fig. 5D). Variation in DNA-binding efficiency would explain both the lower diffusivity and nuclear export rate constant measurements on the ventral side of the embryo. Therefore, we used ccRICS to test this. The amplitude of the CCF, when normalized by the amplitude of the ACF, is a measure of the extent to which Dl-GFP is bound to the DNA. The ratio varied significantly along the DV axis: specifically, it was large on the ventral side and low on the dorsal side. Further, this ratio correlates with the DV asymmetry of our diffusivity measurements. Thus, these results suggest restricted nuclear Dl movement on the ventral side of the embryo correlates with a high proportion of DNA-bound Dl.

Given the possibility that at least two pools of Dl exist in the nucleus (free vs DNA bound), we built a two-component model that accounts for both pools of Dl. Using this model, in conjunction with a one-component model in which all Dl is freely diffusible, we found that lower diffusivities in the one-component model correspond to a large fraction of Dl bound to DNA in our RICS data. In addition, we found the two-component model, compared to the one-component model, fits our data better. While the one-component model gives an estimate of average diffusivity, the two-component model estimates $K_{nuc} = k_{on}/k_{off}$, or, equivalently, the ratio of free Dl to DNA bound Dl. Taken together, our results suggest that there is a DV asymmetry in the efficiency with which Dl can bind to the DNA. On the ventral side of the embryo, a significant fraction of Dl binds DNA, which is correlated with a low diffusivity of nuclear Dl, and likely contributes to a low nuclear export rate constant. In contrast, on the dorsal side, the very small amount of nuclear Dl binds the DNA at a low frequency, and also has a high diffusivity and nuclear export rate.

What could be causing the DV variation in Dl mobility and Dl/DNA interactions (Fig. 5E,F)? One possibility is the Toll-mediated phosphorylation of Dl on the ventral side of the embryo (Fig. 5F). Accordingly, Toll signaling not only disrupts Dl/Cact complex, but also phosphorylates Dl to potentiate its entry into the nucleus (Drier et al., 2000, 1999; Gillespie and Wasserman, 1994; Whalen and Steward, 1993). Thus, at least in part, Toll signaling likely explains the lower nuclear export rate constant on the ventral side. In support of this, our mutant analysis shows that the DV gradient in Dl movement correlates with the Toll signaling gradient. On the other hand, if a significant fraction of Dl is immobilized on the ventral side, this would entail a lower value for the measured nuclear export rate and movement index, which implies that Dl/DNA interactions are also likely to play a part in the lowered nuclear export rate. And while it is possible that phosphorylated Dl, in addition to its higher affinity for the nucleus, also gains a higher affinity for DNA binding (and thus has a slower mobility on the ventral side), no support for such an altered affinity for DNA has been previously shown.

Therefore, we propose that, in addition to Toll signaling possibly reducing the nuclear export rate on the ventral side, the presence of Dl-GFP/Cact complex in the nuclei on the dorsal side of the embryo may reduce the Dl/DNA binding (and thus, increase average Dl diffusivity), as well as increase the measured nuclear export rate (Fig. 5E). If nuclear Dl on the dorsal side is free Dl, and not Dl/Cact complex, then it should have the same ability to bind DNA as free Dl in ventral nuclei, and thus the mobility should be the same. However, if the predominant species in the dorsal-most nuclei is Dl/Cact complex, then it would have high average mobility, owing to the fact that it cannot bind DNA (Geisler et al., 1992; Kidd, 1992). Accordingly, our recent modeling work has shown that the presence of Dl/Cact complex in the nuclei explains the dynamics of Dl-Venus measurements, as well as downstream gene expression, while free Dl alone cannot (Liberman et al., 2009; O'Connell and Reeves, 2015; Reeves et al., 2012). In comparison, mammalian IκB, the homolog of Cact, enters the nucleus to regulate NF-κB dimers (Hall et al., 2006). Furthermore, newly-formed NF-κB/IκB complexes are then rapidly exported from the nuclei; if a similar relationship holds in *Drosophila*, the presence of Dl/Cact complex would also explain the higher nuclear export rate on the dorsal side of the embryo.

Primarily, Cact acts to tether Dl to the cytoplasm and prevent nuclear translocation. Indeed, loss of Cact function permits intermediate levels of Dl to enter the nuclei, even on the dorsal side of the embryo. However, recent secondary, positive roles for Cact in the formation of the Dl gradient have been discovered. Because Cact is degraded on the ventral side of the embryo, there is a DV gradient of Dl/Cact complex, which results in a ventrally-directed net flux of Dl (Carrell et al., 2017). Furthermore, recent experimental work has suggested a pool of Cact fragments, which are refractory to Toll signaling, are able to bind and potentiate Dl signaling on the ventral side of the embryo, possibly through transport as well (Cardoso et al., 2017). In addition to these roles for Cact in establishing the Dl gradient, our proposed mechanism of Cact-mediated regulation of Dl levels inside the nuclei further highlights the multifaceted nature of Cact function. Thus, incorporating quantitative measurements of the Dl/Cact complex should be the next step towards gaining future insights into morphogen signaling and mechanisms required for embryonic patterning.

Materials and Methods

Fly Stocks and Preparation

Drosophila melanogaster stocks were kept on corn meal molasses food in vials or bottles at 25°C and all crosses were performed at 25°C. *Drosophila* embryos, that were about 1-2 hrs old, were collected and mounted on slides for imaging. Briefly, flies were left to deposit eggs on fresh grape juice agar plates with yeast paste for 30-45 min. Those embryos were then aged to 30 min to reach the desired developmental stage. Those embryos are then brushed from the grape juice agar plates into a mesh basket using a paint brush and DI water. The embryos were dechorionated using bleach and then washed with DI water (Carrell & Reeves 2009).

dl-mGFP (Dl-GFP) was created by BAC recombineering and *dl1.2.5* flies were generated by cleaning up *dl1* via two homologous recombinations with *yw* (Carrell et al. 2017). Flies carrying *dl1.2.5* were crossed to flies carrying H2A-RFP on the second chromosome (BS# 23651) to generate flies that have *dl1.2.5,*H2A-RFP transgene on the second chromosome. H2ARFP,*dl1.2.5,dl-mGFP* flies were created by homologous recombination (Carrell et al. 2017). The generation of $Toll^{r4}$ and $Toll^{10B}$ mutant embryos has been previously described (Stathopoulos et al. 2002). Other *Drosophila* strains were obtained from the Bloomington (BL) stock center, namely pll^2 (BL3111) and pll^7 (BL3112).

Mounting and Imaging of Drosophila embryos

Drosophila embryos that were 1-2 hrs old were mounted laterally on a microscope slide using a mixture of heptane glue (Supatto et al. 2009) and two pieces of double-sided tape to prevent sample movement (Carrell & Reeves 2015). Embryos were imaged on a Zeiss LSM 710 confocal microscope using a 40x 1.2NA water objective. Embryos in nuclear cycle 12 to 14 were selected using the H2A-RFP marker. Embryos undergoing cell division (as visualized by the H2A-RFP marker) were not used in for analysis as cell division alters the endogenous Dl distribution.

For image acquisition consistent with RICS analysis, a 256 x 256 pixel region of interest of the embryo was selected for measurements (Supplemental Figure 1). The pixel size of the region varied from 40nm to 100nm to include different numbers of nuclei. The 488nm (green) laser intensity ranged from 0.5% to 3.0% and the 570nm (red) laser intensity ranged from 0.1% to 0.2%. The region of interest was raster scanned with a pixel dwell time of 6.30us for 200 frames (total imaging time of approximately 1.5 minutes). The range of imaging parameters is reported in Table S1.

For image acquisition consistent with pCF analysis, a 32x1 line scan through 2 to 4 nuclei was used as the region of interest (Fig. 2A). The pixel size was not set for each image but, instead, varied between 40-100nm according to the region of interest selected. The laser intensities varied as in the RICS imaging. The line was scanned with a pixel dwell time of 6.30us for 200,000 to 400,000 time points (total imaging time of approximately 1.5 to 3 minutes). The range of imaging parameters is reported in Table S1.

In the photobleaching experiments, embryos were dechorionated, mounted, and imaged using the same protocol as described above. Individual nuclei were chosen at random across the embryo. The following parameters were kept constant: bleaching box, ~700 pixels (26.46 microns by 26.46 microns); bleaching time (amount of time the laser bleached the nuclei), ~20 seconds; number of cycles, 30; and 488nm laser power, 50%. Each bleaching session lasted about 30 minutes (Movie S3) and was followed by imaging the entire depth of the embryo. Two nuclei per embryo were imaged in a single session.

Raster Image Correlation Spectroscopy (RICS) analysis using MATLAB implementation

Analysis of time series images consistent with RICS analysis is briefly described here (see Supplementary Experimental Procedures for more information). First, for each frame i (of size 256×256 pixels) in the Dl-GFP channel, a background subtraction by the average of a sliding window with a five-frame radius was performed to remove the effect of global movement of large structures (Digman et al., 2005b). Next, the average intensity of every pixel in the sliding window was added back to frame i to ensure the frame intensity was not near zero, to yield array I. Finally, to obtain the ACF for frame i, we computed the following for all pixel shifts ξ, η:

$$G_i(\xi, \eta) = \frac{\langle I(x,y)I(x+\xi, y+\eta) \rangle}{\langle I(x,y) \rangle^2}, \qquad (1)$$

where the angle brackets denote ensemble average in both x and y. In practice, $G_i(\xi, \eta)$ is evaluated using the fast Fourier transform method (Digman and Gratton, 2011). The final ACF for total RICS, $G_s(\xi, \eta)$, was computed as the average of $G_i(\xi, \eta)$ for all frames i in the time series. Cross-correlation functions were computed in a similar way, except $I(x+\xi, y+\eta)$ was replaced by the analogous array from the H2A-RFP channel.

To compute nuclear RICS, first a nuclear mask for each frame was found. First, noise and small regions of high intensity that were not nuclei were removed from the H2A-RFP channel through morphological erosion then morphological dilation, followed by Gaussian filtering. Next, the top and bottom 2% of pixels were saturated. Hard thresholds were then applied to find objects presumed to be the nuclei. Finally, due to the previous morphological erosion operation, segmented objects were grown through morphological dilation, resulting in the nuclear mask used for nuclear RICS. The cytoplasmic mask was then found by first taking the complement of the nuclear mask, then eroding the cytoplasmic regions.

The nuclear RICS analysis proceeded the same as that for total RICS, except for each frame, the pixels outside the nuclear mask were set to zero. The resulting $G_i(\xi, \eta)$ were normalized by an array resulting from the application of Eqn (1) to the nuclear mask instead of to array I. The ACF for cytoplasmic RICS was computed analogously.

ACFs calculated from the total, nuclear, or cytoplasmic data were fit to a one component diffusion model (Fig. 1D-F; Digman et al., 2005b):

$$G_s^{model}(\xi, \eta; A, B, D) = \frac{A \exp\left(-\frac{(r/w_0)^2}{1 + 4D\,\tau/w_0^2}\right)}{(1 + 4D\,\tau/w_0^2)\sqrt{1 + 4D\,\tau/w_z^2}}, \qquad (2)$$

where $r = \Delta r \sqrt{\xi^2 + \eta^2}$, $\tau = \tau_p \xi + \tau_\ell \eta$, Δr is the pixel size in microns, τ_p and τ_ℓ are the pixel dwell time and line scan time in seconds, respectively, and w_0 and w_z are the waist sizes of the point spread function in the planar and axial directions, respectively. Equation (2) was fit to $G_s(\xi, \eta)$ using least squares and varying A, B, D. The parameters $\Delta r, \tau_p, \tau_\ell, w_0, w_z$ were

microscope parameters and considered fixed. ACFs calculated from the nuclear data were fit to two-component and three-component models in the least squares sense (Fig. 4D,E). The derivation and application of these models can be found in the Supplementary Experimental Procedures.

Pair Correlation Function (pCF) analysis using SimFCS software

pCF analysis of the collected line scans was performed using the SimFCS software (Digman et al, 2005; https://www.lfd.uci.edu/globals/) as described in Clark and Sozzani, 2017. Three pixel distances of 6, 7, and 8 pixels were used as technical replicates to account for differences in sizes of nuclei. If Dl-GFP showed movement out of/into a majority of nuclei (no black region or black arch in the pCF carpet), that image was assigned a movement index of 1. Otherwise, if the majority of Dl-GFP showed no movement (black vertical region in the pCF carpet), that image was assigned a movement index of 0 (Fig. 2A). The 3 technical replicates were then averaged for each biological replicate. The analysis was repeated for the line scan in the reverse direction, resulting in 6 total technical replicates per image.

Fluorescence Recovery After Photobleaching (FRAP) Analysis

Each FRAP experiment was analyzed according to the following procedure (see Supplementary Experimental Procedures for more information). First, the image sequence was stabilized using a standard optical flow protocol, which was necessary because the embryo sometimes moved very slightly during imaging (see Supplementary Experimental Procedures; Carrell et al., 2017). Next, the H2A-RFP channel was segmented to find the nuclei and cytoplasm in a manner similar to the RICS images (see Supplementary Experimental Procedures for more information and relevant differences). The intensity of Dl-GFP in the bleached nucleus was fit to a differential equation that describes nuclear import and export of Dl-GFP (see Supplementary Experimental Procedures; Carrell et al., 2017), which yielded estimates of the nuclear import rate constant, k_{in}, and the import/export equilibrium constant, $K_{nuc} \equiv k_{in}/k_{out}$.

Mathematical models of nuclear Dorsal and DNA binding

In the two-component model (see Fig. 4), we assume Dl is present in the nucleus in two states in equilibrium: bound to DNA and unbound. Unbound Dl is free to diffuse in the nucleus with diffusivity of 2.3 μm²/s, while DNA-bound Dl is immobile. Dl can bind to DNA with a binding rate constant of k'_{on} and dissociates from the DNA with rate constant k_{off} = 0.025 s^{-1}. We varied $K_{DNA} \equiv k'_{on}/k_{off}$, which is related to φ, the fraction of Dl that is unbound, from near infinity to near zero. See Supplementary Experimental Procedures for more details.

Quantification and statistical analysis

Non-linear least squares was used to fit Equation (2) to the RICS ACFs. The fitted diffusivity value is t-distributed, and a standard error for the diffusivity (radius of a 68% confidence interval) was calculated. With the exception of five time course image stacks of nuclear RICS either on the dorsal side of wild type embryos, or in $pll^{2/7}$ embryos (the two cases in which nuclear intensity is

very low), for all fitted diffusivities, the standard error was less than 4 μm^2/s. This was used as a filter for the data; the five time course image stacks in which the standard error was greater than 4 μm^2/s were removed from analysis.

For the diffusivity of Dl calculated by RICS (Fig. 1D-F), the ccRICS data (ratio of amplitudes; Fig. 3C,D), and for the correlation between nuclear diffusivity and φ (Fig. 4E), simple linear least squares regression was applied. The slope of the regression trend line is t-distributed with n-2 degrees of freedom, where n is the number of data points. Reported p-values are for t-tests with the null hypothesis that the slope is zero.

For the pCF data (Fig. 2), a Chi-squared test with likelihood ratio was used to test if the proportion of Movement Index (MI) values that were less than 0.5 was different for movement measured into the nucleus vs movement measured out of the nucleus. The Chi-squared test was performed using JMP software (https://www.jmp.com/).

The FRAP data (Fig. 2C,D) was tested for significance by t-test. The null hypothesis was that the rate constant of nucleocytoplasmic shuttling (k_{in} or k_{out}) did not differ between ventral and dorsal sides.

For all tests, a p-value less than 0.05 was considered significant, and for the Chi-Squared test we also consider the two p-values that were less than 0.07 as significant (Fig. 2). The statistical tests performed on each sample are listed in the Results text as well as the figure legends. Sample sizes are indicated on the figures. Means and standard errors are reported in the Results.

Data and software availability

Images, tables, and sequencing results will be uploaded to a data repository, Data Dryad. Accession numbers will be available upon notification of acceptance for publication. Matlab codes will be uploaded to NCSU resource github.ncsu.edu and will also be available from the Reeves Lab website.

References

Aldaz, S., Escudero, L.M., and Freeman, M. (2010). Live imaging of Drosophila imaginal disc development. Proc Natl Acad Sci U S A *107*, 14217–14222.

Anderson, K. V, and Nüsslein-Volhard, C. (1984). Information for the dorsal--ventral pattern of the Drosophila embryo is stored as maternal mRNA. Nature *311*, 223–227.

Anderson, K. V, Jürgens, G., and Nüsslein-Volhard, C. (1985a). Establishment of dorsal-ventral polarity in the Drosophila embryo: Genetic studies on the role of the Toll gene product. Cell *42*, 779–789.

Anderson, K. V, Bokla, L., and Nüsslein-Volhard, C. (1985b). Establishment of dorsal-ventral polarity in the Drosophila embryo: the induction of polarity by the Toll gene product. Cell *42*, 791–798.

Ashe, H.L., and Briscoe, J. (2006). The interpretation of morphogen gradients. Development

133, 385–394.

Belvin, M.P., and Anderson, K. V. (1996). A CONSERVED SIGNALING PATHWAY: The Drosophila Toll-Dorsal Pathway. Annu. Rev. Cell Dev. Biol. *12*, 393–416.

Belvin, M.P., Jin, Y., and Anderson, K. V (1995). Cactus protein degradation mediates Drosophila dorsal-ventral signaling. Genes Dev *9*, 783–793.

Bergmann, A., Stein, D., Geisler, R., Hagenmaier, S., Schmid, B., Fernandez, N., Schnell, B., and Nüsslein-Volhard, C. (1996). A gradient of cytoplasmic Cactus degradation establishes the nuclear localization gradient of the dorsal morphogen in Drosophila. Mech. Dev. *60*, 109–123.

Cardoso, M.A., Fontenele, M., Lim, B., Bisch, P.M., Shvartsman, S.Y., and Araujo, H.M. (2017). A novel function for the IκB inhibitor Cactus in promoting Dorsal nuclear localization and activity in the Drosophila embryo. Development *144*, 2907–2913.

Carrell, S.N., O'Connell, M.D., Jacobsen, T., Pomeroy, A.E., Hayes, S.M., and Reeves, G.T. (2017). A facilitated diffusion mechanism establishes the Drosophila Dorsal gradient. Development *144*, 4450–4461.

Chopra, V.S., and Levine, M. (2009). Combinatorial patterning mechanisms in the Drosophila embryo. Brief. Funct. Genomic. Proteomic. *8*, 243–249.

Daigneault, J., Klemetsaune, L., and Wasserman, S.A. (2013). The IRAK homolog Pelle is the functional counterpart of IκB kinase in the Drosophila Toll pathway. PLoS One *8*, e75150.

Delotto, R., Delotto, Y., Steward, R., and Lippincott-schwartz, J. (2007). Nucleocytoplasmic shuttling mediates the dynamic maintenance of nuclear Dorsal levels during Drosophila embryogenesis. Development *4241*, 4233–4241.

Digman, M.A., and Gratton, E. (2009). Imaging barriers to diffusion by pair correlation functions. Biophys J *97*, 665–673.

Digman, M.A., and Gratton, E. (2011). Lessons in fluctuation correlation spectroscopy. Annu. Rev. Phys. Chem. *62*, 645–668.

Digman, M.A., Brown, C.M., Sengupta, P., Wiseman, P.W., Horwitz, A.R., and Gratton, E. (2005a). Measuring fast dynamics in solutions and cells with a laser scanning microscope. Biophys J *89*, 1317–1327.

Digman, M.A., Sengupta, P., Wiseman, P.W., Brown, C.M., Horwitz, A.R., and Gratton, E. (2005b). Fluctuation correlation spectroscopy with a laser-scanning microscope: exploiting the hidden time structure. Biophys J *88*, L33--L36.

Digman, M.A., Wiseman, P.W., Horwitz, A.R., and Gratton, E. (2009). Detecting protein complexes in living cells from laser scanning confocal image sequences by the cross correlation raster image spectroscopy method. Biophys J *96*, 707–716.

Dresch, J.M., Thompson, M.A., Arnosti, D.N., and Chiu, C. (2013). Two-Layer Mathematical Modeling of Gene Expression: Incorporating DNA-Level Information and System Dynamics. SIAM J Appl Math *73*, 804–826.

Drier, E.A., Govind, S., and Steward, R. (2000). Cactus-independent regulation of Dorsal nuclear import by the ventral signal. Curr. Biol. *10*, 23–26.

Drier, E. a, Huang, L.H., and Steward, R. (1999). Nuclear import of the Drosophila Rel protein Dorsal is regulated by phosphorylation. Genes Dev. *13*, 556–568.

Entchev, E. V, Schwabedissen, A., and González-Gaitán, M.A. (2000). Gradient formation of the {TGF}-beta homolog {D}pp. Cell *103*, 981–991.

Geisler, R., Bergmann, A., Hiromi, Y., and Nüsslein-Volhard, C. (1992). cactus, a gene involved in dorsoventral pattern formation of Drosophila, is related to the I kappa B gene family of vertebrates. Cell *71*, 613–621.

Gillespie, S.K.H., and Wasserman, S.A. (1994). dorsal , a Drosophila Rel-Like Protein , Is Phosphorylated upon Activation of the Transmembrane Protein Toll. Reactions *14*, 3559–3568.

Gregor, T., Wieschaus, E.F., McGregor, A.P., Bialek, W., and Tank, D.W. (2007). Stability and nuclear dynamics of the Bicoid morphogen gradient. Cell *130*, 141–152.

Gurdon, J.B., and Bourillot, P.Y. (2001). Morphogen gradient interpretation. Nature *413*, 797–803.

Gurdon, J.B., Mitchell, a, and Mahony, D. (1995). Direct and continuous assessment by cells of their position in a morphogen gradient. Nature *376*, 520–521.

Hall, G., Hasday, J.D., and Rogers, T.B. (2006). Regulating the regulator: NF-κB signaling in heart. J. Mol. Cell. Cardiol. *41*, 580–591.

Hinde, E., Cardarelli, F., Digman, M.A., and Gratton, E. (2010). In vivo pair correlation analysis of EGFP intranuclear diffusion reveals DNA-dependent molecular flow. Proc Natl Acad Sci U S A *107*, 16560–16565.

Holzer, T., Liffers, K., Rahm, K., Trageser, B., Özbek, S., and Gradl, D. (2012). Live imaging of active fluorophore labelled Wnt proteins. FEBS Lett. *586*, 1638–1644.

Jaeger, J., Surkova, S., Blagov, M., Janssens, H., Kosman, D., Kozlov, K.N., Manu, Myasnikova, E., Vanario-Alonso, C.E., Samsonova, M., et al. (2004). Dynamic control of positional information in the early \textit{{D}rosophila} embryo. Nature *430*, 368–371.

Kidd, S. (1992). Characterization of the Drosophila cactus locus and analysis of interactions between cactus and dorsal proteins. Cell *71*, 623–635.

Liberman, L.M., Reeves, G.T., and Stathopoulos, A. (2009). Quantitative imaging of the Dorsal nuclear gradient reveals limitations to threshold-dependent patterning in Drosophila. Proc. Natl. Acad. Sci. U. S. A. *106*, 22317–22322.

Luz, M., Spannl-Müller, S., Özhan, G., Kagermeier-Schenk, B., Rhinn, M., Weidinger, G., and Brand, M. (2014). Dynamic Association with Donor Cell Filopodia and Lipid-Modification Are Essential Features of Wnt8a during Patterning of the Zebrafish Neuroectoderm. PLoS One *9*, e84922.

Mavrakis, M., Pourquie, O., and Lecuit, T. (2010). Lighting up developmental mechanisms: how fluorescence imaging heralded a new era. Development *137*, 373–387.

Moussian, B., and Roth, S. (2005). Dorsoventral axis formation in the Drosophila embryo-- shaping and transducing a morphogen gradient. Curr. Biol. *15*, R887--R899.

O'Connell, M.D., and Reeves, G.T. (2015). The Presence of Nuclear Cactus in the Early Drosophila Embryo May Extend the Dynamic Range of the Dorsal Gradient. PLOS Comput. Biol. *11*, e1004159.

Oates, A.C., Gorfinkiel, N., González-Gaitán, M., and Heisenberg, C.-P. (2009). Quantitative approaches in developmental biology. Nat Rev Genet *10*, 517–530.

Pantazis, P., and Supatto, W. (2014). Advances in whole-embryo imaging: a quantitative transition is underway. Nat Rev Mol Cell Biol *15*, 327–339.

Reach, M., Galindo, R.L., Towb, P., Allen, J.L., Karin, M., and Wasserman, S.A. (1996). A gradient of cactus protein degradation establishes dorsoventral polarity in the Drosophila embryo. Dev. Biol. *180*, 353–364.

Reeves, G.T., and Stathopoulos, A. (2009). Graded dorsal and differential gene regulation in the Drosophila embryo. Cold Spring Harb Perspect Biol *1*, a000836.

Reeves, G.T., Kalifa, R., Klein, D.E., Lemmon, M.A., and Shvartsman, S.Y. (2005). Computational analysis of EGFR inhibition by Argos. Dev. Biol. *284*, 523–535.

Reeves, G.T., Trisnadi, N., Truong, T. V, Nahmad, M., Katz, S., and Stathopoulos, A. (2012).

Dorsal-ventral gene expression in the Drosophila embryo reflects the dynamics and precision of the dorsal nuclear gradient. Dev. Cell *22*, 544–557.

Ribes, V., Balaskas, N., Sasai, N., Cruz, C., Dessaud, E., Cayuso, J., Tozer, S., Yang, L.L., Novitch, B., Marti, E., et al. (2010). Distinct Sonic Hedgehog signaling dynamics specify floor plate and ventral neuronal progenitors in the vertebrate neural tube. Genes Dev. *24*, 1186–1200.

Roth, S., Stein, D., and Nüsslein-Volhard, C. (1989). A gradient of nuclear localization of the dorsal protein determines dorsoventral pattern in the Drosophila embryo. Cell *59*, 1189–1202.

Roth, S., Hiromi, Y., Godt, D., and Nüsslein-Volhard, C. (1991). cactus, a maternal gene required for proper formation of the dorsoventral morphogen gradient in Drosophila embryos. Development *112*, 371–388.

Schneider, D.S., Hudson, K.L., Lin, T.Y., and Anderson, K. V (1991). Dominant and recessive mutations define functional domains of Toll, a transmembrane protein required for dorsal-ventral polarity in the Drosophila embryo. Genes Dev. *5*, 797–807.

Stathopoulos, A., and Levine, M. (2002). Dorsal gradient networks in the Drosophila embryo. Dev. Biol. *246*, 57–67.

Stathopoulos, A., and Levine, M. (2004). Whole-genome analysis of Drosophila gastrulation. Curr. Opin. Genet. Dev. *14*, 477–484.

Steward, R. (1987). Dorsal, an embryonic polarity gene in Drosophila, is homologous to the vertebrate proto-oncogene, c-rel. Science (80-.). *238*, 692–694.

Steward, R., Zusman, S.B., Huang, L.H., and Schedl, P. (1988). The dorsal protein is distributed in a gradient in early drosophila embryos. Cell *55*, 487–495.

Teleman, A.A., and Cohen, S.M. (2000). Dpp gradient formation in the \textit{{D}rosophila} wing imaginal disc. Cell *103*, 971–980.

Wallkamm, V., Dörlich, R., Rahm, K., Klessing, T., Nienhaus, G.U., Wedlich, D., and Gradl, D. (2014). Live Imaging of Xwnt5A-ROR2 Complexes. PLoS One *9*, e109428.

Wartlick, O., Mumcu, P., Kicheva, a, Bittig, T., Seum, C., Jülicher, F., and González-Gaitán, M. (2011). Dynamics of Dpp signaling and proliferation control. Science (80-.). *331*, 1154–1159.

Whalen, A.M., and Steward, R. (1993). Dissociation of the Dorsal-Cactus complex and phosphorylation of the Dorsal protein correlate with the nuclear localization of Dorsal. J Cell Biol *123*, 523–534.

Wharton, S.J., Basu, S.P., and Ashe, H.L. (2004). Smad affinity can direct distinct readouts of the embryonic extracellular {D}pp gradient in \textit{{D}rosophila}. Curr Biol *14*, 1550–1558.

Williams, P.H., Hagemann, A., González-Gaitán, M., and Smith, J.C. (2004). Visualizing long-range movement of the morphogen Xnr2 in the Xenopus embryo. Curr Biol *14*, 1916–1923.

Zhou, S., Lo, W.-C., Suhalim, J.L., Digman, M.A., Gratton, E., Nie, Q., and Lander, A.D. (2012). Free Extracellular Diffusion Creates the Dpp Morphogen Gradient of the Drosophila Wing Disc. Curr. Biol. *22*, 668–675.

Figures
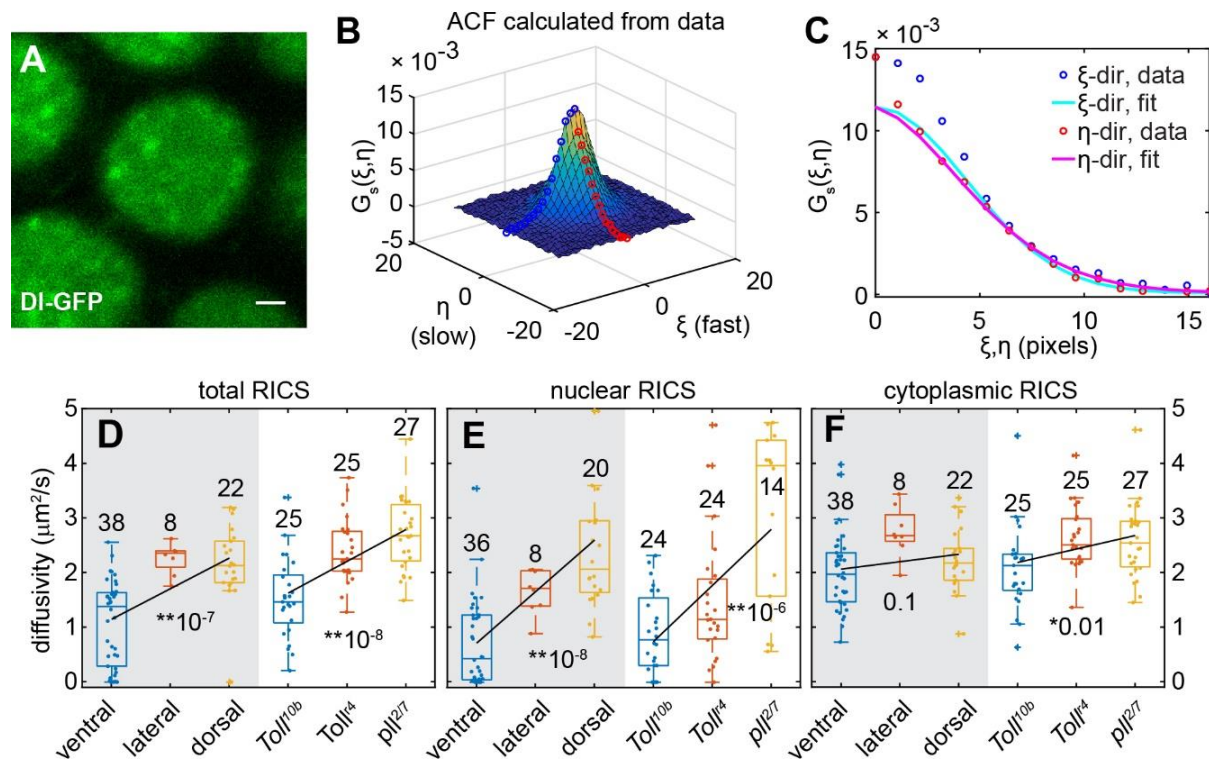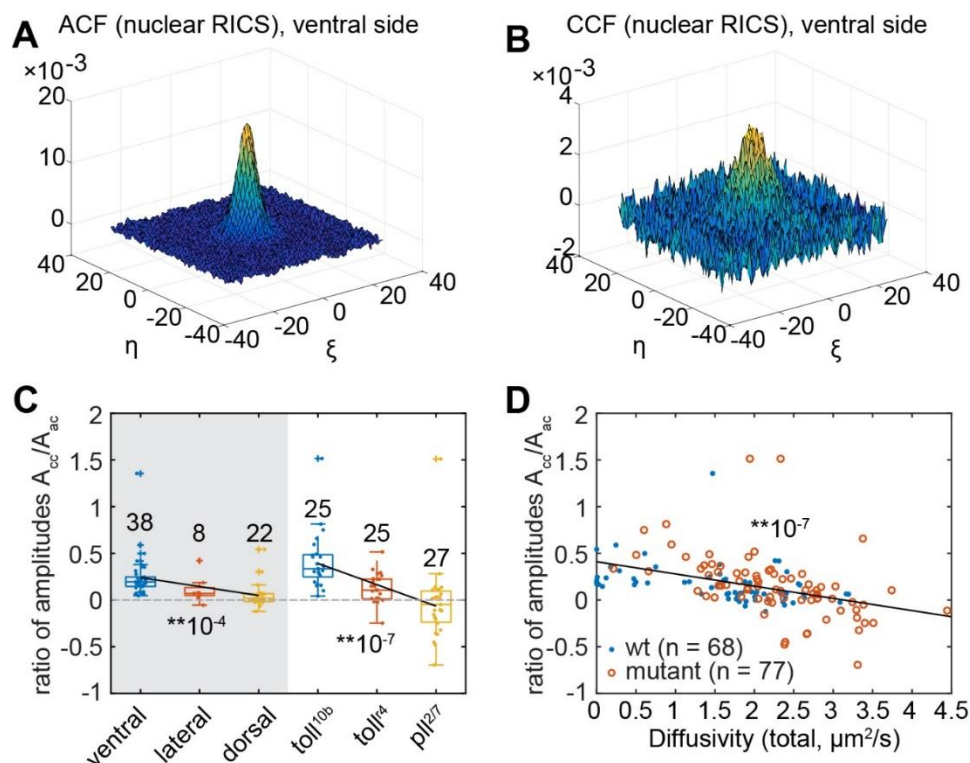

Figure 1: RICS analysis reveals a dorsal-ventral asymmetry in the mobility of Dl. (A) Representative image of Dl-GFP used for RICS analysis. Scale bar = 1 μm. (B,C) Plots of the autocorrelation function (ACF) of the image in A. (B) 3D plot of the ACF. Blue and red open circles represent the slice of the 3D surface for the fast and slow directions, respectively. (C) Plot of the fast and slow slices of the 3D ACF. Blue and red open circles (experimental data) correspond to those found in (B). The experimental data (open circles) are fit using a diffusion model (solid curves). The data and fit are separated into two components, the "fast" (ξ, blue/cyan) and "slow" (η, red/magenta) directions. (D-F) Boxplots of the diffusivity of Dl-GFP measured using RICS on the entire imaging frame (nuclear plus cytoplasmic) (D), nuclear regions only (E), or cytoplasmic regions only (F). The left side of the plots (gray) contains wildtype embryos, while the right side (white) contains mutant embryos. Blue represents ventral/"ventral-like", orange represents lateral/"lateral-like", and yellow represents dorsal/"dorsal-like" measurements. Solid dots represent individual measurements. Black line is a linear regression fitted to the data. *p*-values for the slope of the trendline being zero are indicated on the graph. Sample sizes indicated on graph.

Figure 2: pCF analysis and FRAP reveal a dorsal-to-ventral asymmetry in nuclear export of Dl. (A) Representative images of Dl-GFP on the ventral (top left image) and dorsal (top right image) sides of the embryo with their respective pCF carpets (bottom left and bottom right). Scale bar = 2um. Arrow represents the direction of the line scan. Magenta circles in dorsal side image outline the two nuclei crossed by the line scan. White, dashed line represents areas where Dl-GFP movement is measured out of the nucleus. Orange, dashed lines in the carpet label arches which indicate delayed Dl-GFP movement, while green, solid lines demarcate black regions of the carpet which indicate no Dl-GFP movement. (B) Percent of embryos that have high (Movement Index (MI) > 0.5, orange) and low (MI ≤ 0.5, blue) Dl-GFP movement either out of (out) or into (in) the nucleus. * denotes p<0.07, ** denotes p<0.05, Chi-squared test with likelihood ratio. (C) Representative trace of nuclear (blue) and cytoplasmic (red) Dl-GFP fluorescence in the FRAP experiments. Yellow curve is the fit of the fluorescence recovery equation. (D) Boxplots of the nuclear import (left side, gray background) or export (right side, white background) rate constants measured using FRAP on either the ventral (v) or dorsal (d) regions of the embryo. *p*-values testing if the rate constants on the ventral side are equal those on the dorsal side are indicated on the graph. Sample sizes indicated on graph.
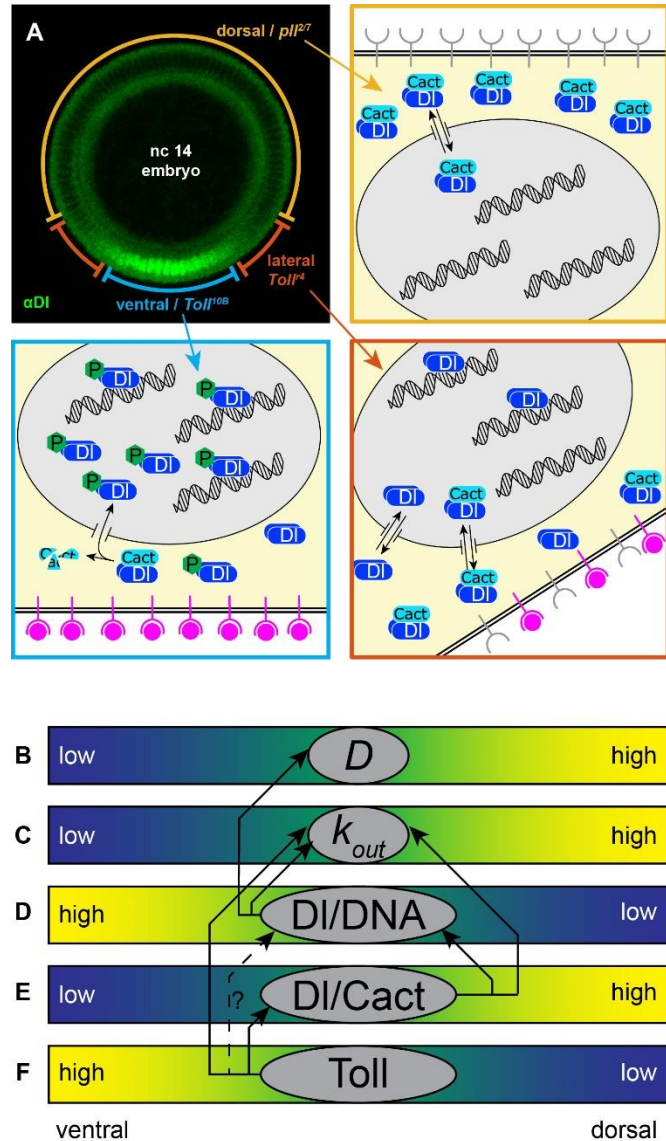
Figure 3: Cross-correlation RICS analysis of DNA-bound Dl. (A) Autocorrelation function of Dl-GFP, with nuclear mask, on ventral side. (B) Cross-correlation between Dl-GFP and H2A-RFP, with nuclear mask, from same image used to calculate (A). (C) Boxplot of the ratio of the cross-correlation amplitude to the autocorrelation amplitude (A_{cc}/A_{ac}). The left side of the plots (gray) contains wildtype embryos, while the right side (white) contains mutant embryos. Blue represents ventral/"ventral-like", orange represents lateral/"lateral-like", and yellow represents dorsal/"dorsal-like" measurements. Solid dots represent individual measurements. Black line is a linear regression fitted to the data. p-values for the slope of the trendline being zero are indicated on the graph. Sample sizes indicated on graph. (D) Plot of the ratio A_{cc}/A_{ac} (y-axis) versus diffusion coefficient returned by RICS (x-axis). Blue solid dots represent measurements from wild type embryos, while red open circles are measurements from mutant embryos. Black line is a linear regression fitted to the data. p-value for the slope of the trendline being zero are indicated on the graph. Sample sizes indicated in legend.
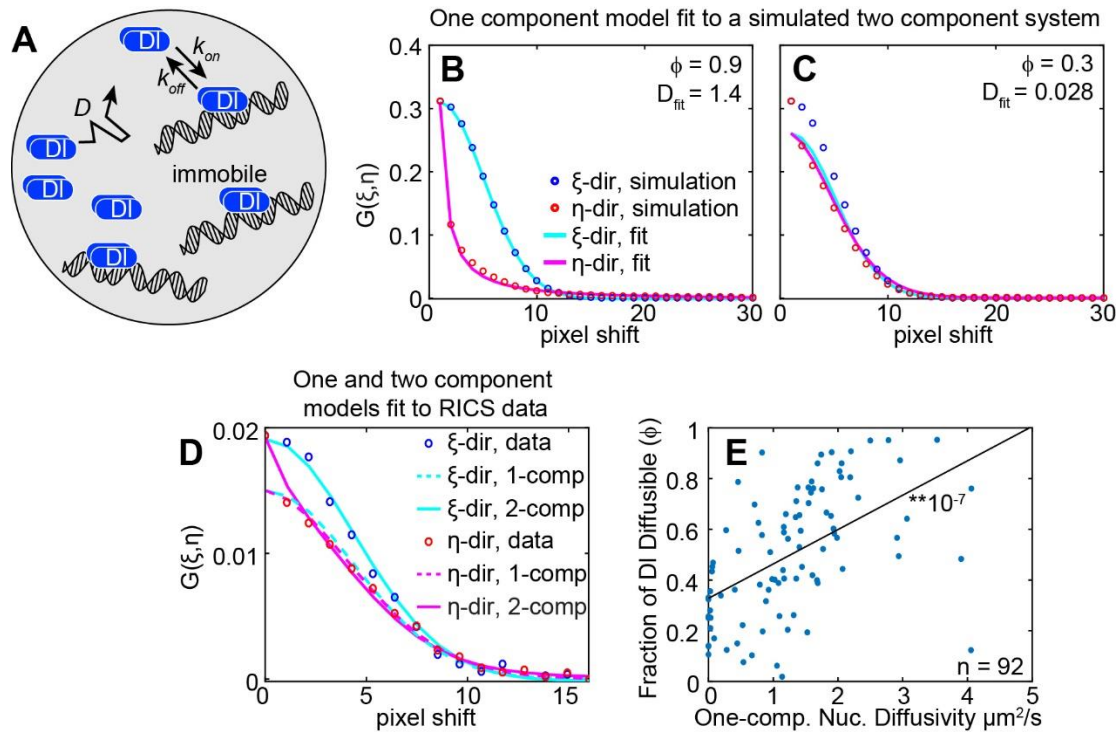
Figure 4: One- and two-component diffusion models quantify the relationship between DNA binding and mobility of Dl. (A) Illustration of the two-component model. Dl (black circles) can diffuse and reversibly bind DNA. Dl bound to DNA is immobile. In contrast to the one-component diffusion model, in which Dl is freely diffusible and does not bind to DNA. (B,C) One-component diffusion model (solid curves) fit to a simulated two-component autocorrelation function (ACF) (open circles) for (B) 90% freely diffusible Dl and 10% DNA-bound Dl (φ =0.9) and (C) 30% freely diffusible Dl and 70% DNA-bound Dl (φ = 0.3). The data and fit are separated into two components, the "fast" (ξ, blue/cyan) and "slow" (η, red/magenta) directions. (D) Comparison of one-component (dashed curves) and two-component (solid curves) diffusion models fit to experimental RICS data (open circles). (E) Plot of the proportion of free Dl (φ, y-axis) versus the diffusion coefficient of free Dl returned from the one-component diffusion model (x-axis). Black line is a linear regression fitted to the data. *p*-value for the slope of the trendline being zero are indicated on the graph. Sample size indicated on graph.

Figure 5: Variation of Dl mobility along the DV axis. (A) (top left) Depiction of the different embryo domains, ventral (blue region), lateral (orange region), and dorsal (yellow region). (bottom left) Schematic of ventral side of embryo. High levels of activated Toll (magenta receptors) result in the destruction of Cact and phosphorylation of Dl. Free Dl enters the nucleus, so GFP fluorescence is mostly nuclear. Free Dl in the nucleus binds to DNA, which lowers the overall mobility of Dl species, and exits the nucleus at a slow rate. (bottom right) Schematic of lateral domain of embryo. Lower levels of Toll activation lead to a mixture of free and Cact-bound Dl. Nuclear and cytoplasmic levels of GFP fluorescence are roughly equal. Dl has a higher mobility due to lower fraction of Dl bound to the DNA. Dl exits the nucleus faster than on the ventral side. (top right) Schematic of the dorsal domain of the embryo. Little-to-no free Dl is present, so Dl-GFP fluorescence is mostly cytoplasmic. High mobilities stem from no DNA binding. (B-E) Graphical summary of the DV asymmetry in the data. (B,C) Both diffusivity (one-component RICS measurement) and nuclear export rate constant (one component bleaching recovery model) are low on the ventral side and high on the dorsal side. (D) The binding efficiency between Dl and DNA is high on the ventral side and low on the dorsal side. We propose that Dl/DNA binding is partially responsible for the DV asymmetry in both the diffusivity and nuclear export rate measurements. (E) We propose that the presence of Dl/Cact complex in the nucleus (low on ventral side; high on dorsal side) contributes to the lack of Dl/DNA binding, as well as the higher nuclear export rate on the dorsal side. (F) Toll signaling (high on ventral side; low on dorsal side) also likely plays a significant part in the DV asymmetry in the nuclear export rate and may also contribute to the DV asymmetry in Dl/DNA binding, in addition to its primary function to limit Dl/Cact complex on the ventral side.